NANO EXPRESS　　　　　　　　　　　　　　　　　　**Open Access**

Enhanced photoelectrocatalytic performance of α-Fe$_2$O$_3$ thin films by surface plasmon resonance of Au nanoparticles coupled with surface passivation by atom layer deposition of Al$_2$O$_3$

Yuting Liu[1,2], Zhen Xu[2], Min Yin[2*], Haowen Fan[1], Weijie Cheng[1,2], Linfeng Lu[2], Ye Song[1], Jing Ma[3*] and Xufei Zhu[1]

Abstract

The short lifetime of photogenerated charge carriers of hematite (α-Fe$_2$O$_3$) thin films strongly hindered the PEC performances. Herein, α-Fe$_2$O$_3$ thin films with surface nanowire were synthesized by electrodeposition and post annealing method for photoelectrocatalytic (PEC) water splitting. The thickness of the α-Fe$_2$O$_3$ films can be precisely controlled by adjusting the duration of the electrodeposition. The Au nanoparticles (NPs) and Al$_2$O$_3$ shell by atom layer deposition were further introduced to modify the photoelectrodes. Different constructions were made with different deposition orders of Au and Al$_2$O$_3$ on Fe$_2$O$_3$ films. The Fe$_2$O$_3$-Au-Al$_2$O$_3$ construction shows the best PEC performance with 1.78 times enhancement by localized surface plasmon resonance (LSPR) of NPs in conjunction with surface passivation of Al$_2$O$_3$ shells. Numerical simulation was carried out to investigate the promotion mechanisms. The high PEC performance for Fe$_2$O$_3$-Au-Al$_2$O$_3$ construction electrode could be attributed to the Al$_2$O$_3$ intensified LSPR, effective surface passivation by Al$_2$O$_3$ coating, and the efficient charge transfer due to the Fe$_2$O$_3$-Au Schottky junctions.

Keywords: Hematite; Photoelectrocatalytic water splitting; Surface plasmon resonance; Surface passivation; Atomic layer deposition

Background

Solar water splitting has received great attention because of the potential of the mass production of green and renewable fuel [1–3]. The visible-light-active photocatalysts is envisioned to be successful for this application [4]. α-Fe$_2$O$_3$ (hematite) with low band gap (Eg = ~2.2 eV), natural abundance, low cost, and excellent chemical stability is one of the promising metal oxide semiconductor materials for this application [5]. It has been theoretically predicted that a semiconductor with this band gap can achieve a solar-to-hydrogen efficiency of 16.8 % [6]. However, the reported efficiencies of α-Fe$_2$O$_3$ are notoriously lower than the predicted value, mainly due to the short lifetime of photogenerated charge carriers (<10 ps) [7–9], whereas the absorption depth of 2.2 eV photons (near the band gap) in hematite (118 nm) is much larger than the diffusion distance (2 ~ 4 nm) [10]. In this regard, very thin α-Fe$_2$O$_3$ films should be used for facilitating the carriers transport and collection. It is significantly crucial and challenging to make the thin film electrode possess efficient absorption for effective photoelectrocatalytic (PEC) water splitting.

Surface plasmon is an efficient method to localize photon absorption at the semiconductor surface through incorporation of plasmonic metal nanoparticles on the semiconductor electrode [11, 12]. Au is an attractive plasmonic metal for PEC water splitting [13], which cannot only interact with the incident light in visible and infrared region but also act as an electron trap facilitating electron–hole

* Correspondence: yinm@sari.ac.cn; jingma@shu.edu.cn
[2]Shanghai Advanced Research Institute, Chinese Academy of Sciences, Shanghai 201210, China
[3]School of Environmental and Chemical Engineering, Shanghai University, Shanghai 200444, China
Full list of author information is available at the end of the article

Liu *et al. Nanoscale Research Letters* (2015) 10:374

Page 2 of 8

separation by forming local Schottky junctions. The plasmon resonance frequency and intensity depends on the geometry and distribution engineering of nanoparticles and also the dielectric property of the surrounding medium.

Surface passivation of semiconductors could efficiently reduce the surface charge recombination in semiconductor technology, which is of significant importance on enhanced performances. The atomic layer deposition (ALD) is a common and easy surface modification method that has been employed in solar cells [14, 15], water splitting [16, 17], and solar fuel production [18, 19]. ALD is a stepwise and conformal coating technique with precisely controlled composition and thickness with a few nanometers. Our recent work demonstrated that 0.8 -fold enhancement of photocurrent was achieved by coating TiO_2 nanotubes with Al_2O_3 [17].

Therefore, it is accordingly hopeful to construct novel structured α-Fe_2O_3 electrode with high solar-to-hydrogen efficiency by integrating the surface plasmon resonance and surface passivation on α-Fe_2O_3. In this paper, α-Fe_2O_3 thin films with surface nanowire were realized by an electrodeposition and post thermally annealing process. Further, Au NPs and Al_2O_3 thin layers were loaded on the surface of the α-Fe_2O_3 to explore the PEC performance of α-Fe_2O_3. Different constructions were achieved with different deposition orders of Au and Al_2O_3. Numerical simulations by finite difference time domain (FDTD) method were employed to investigate the effect of Au and Al_2O_3 coating on α-Fe_2O_3 electrodes.

Methods

Synthesis of α-Fe_2O_3

Fluorine-modified tin oxide (FTO)-coated glasses were immersed in isopropanol with saturated KOH solution for 24 h to remove absorbed organics, followed by ultrasonically cleaned in acetone, ethanol, and distilled water successively for 25 min. Fe films were prepared by constant current (20 mA $\cdot$ cm^{-2}) electrodeposition on the FTO for 120, 180, and 360 s. The deposition solution consists of 48 g ferrous sulfate ($FeSO_4 \cdot 7H_2O$, ≥99.0 %, Greagent), 1.2 g ascorbic acid ($C_6H_8O_6$, ≥99.7 %, Greagent), 0.4 g amidosulfonic acid (H_2NSO_3H, ≥99.0 %, Greagent), 12 g boric acid (H_3BO_3, ≥99.5 %, Greagent), and 800 mL distilled water. Electrodeposition was carried out in a standard three-electrode configuration consisting of a Pt foil counter electrode, an Ag/AgCl reference electrode (saturated by 3 M KCl), and a FTO working electrode. After electrodeposition, the α-Fe_2O_3 films will be formed by post annealing process in the muffle furnace immediately at 150 °C for 2 h then up to 520 °C for 4 h with a heating rate of 2 °C$\cdot$min^{-1}.

Loading of Au nanoparticles

The Au films were deposited on the Fe_2O_3 electrodes using an ion sputtering equipment (DENTON VACUUM/ DESK V HP) with the current of 30 mA $\cdot$ cm^{-2} for different sputtered time (10, 15, 25, 35 s). The vacuum degree during ion sputtering was lower than 0.099 Torr. The Fe_2O_3 electrode modified with nanoparticles (NPs) was denoted as Fe_2O_3-Au. Then Fe_2O_3-Au electrode was annealed in ambient air at 300 °C for 1 h in a rapid thermal annealing furnace to form Au spheres on the surface of Fe_2O_3 [20, 21].

Conformal coating of Al_2O_3

Al_2O_3 shells were conformally coated onto the Fe_2O_3 or Fe_2O_3-Au by ALD processes performed with SUNALETMR-200. Al_2O_3 shells were deposited at 200 °C for 25 cycles using $Al(CH_3)_3$ and H_2O as precursors with a growth rate of ~1 Å$\cdot$cycle^{-1}. Thus, a series of composite nanostructures based on Fe_2O_3 films, i.e., Fe_2O_3, Fe_2O_3-Al_2O_3, Fe_2O_3-Au, Fe_2O_3-Au-Al_2O_3, and Fe_2O_3-Al_2O_3-Au had been constructed.

Characterization

The morphology and crystalline structure of the electrodes was characterized by field-emission scanning electron microscope (FESEM, Hitachi S4800) and X-ray diffractometer (XRD, Bruker D8 Discover diffractometer), respectively.

The PEC water splitting performances of the Fe_2O_3 based electrodes were evaluated by AUTOLAB (PGSTAT302N/FRA2) using a three-electrode setup with the Fe_2O_3-based films (1 cm^2) as working electrode, Ag/AgCl (3 M KCl) electrode as reference electrode, and a platinum foil as counter electrode following our previous work [22]. Used as the supporting electrolyte was 1 M KOH solution. The Al_2O_3 layer deposited by ALD method is stable in the KOH solution [23]. The photocurrent was measured at an applied potential of 0.4 V vs Ag/AgCl under chopped light irradiation with a Xe lamp (PLS-SXE300UV) coupled with an AM 1.5G filter. The light was achieved irradiated to the backside of the electrodes (FTO side, backside illumination). The electrochemical impedance spectroscopy measurements were performed in dark at open circuit potential over a frequency ranging from 100000 to 0.1 Hz with amplitude of 10 mV. The Mott-Schottky plots were obtained at a fixed frequency of 1 kHz.

Results and discussion

Figure 1a, b shows the digital photographs of Fe film with 180 s electrodeposition and Fe_2O_3 film after annealing process. The Fe film has a matt black color with good uniformity. Annealing treatment yields the formation of oxide film with red color. Figure 1c shows the XRD patterns of the Fe and Fe_2O_3 film. The crystallite diffractions of SnO_2 from FTO were labeled as solid circle. The XRD pattern
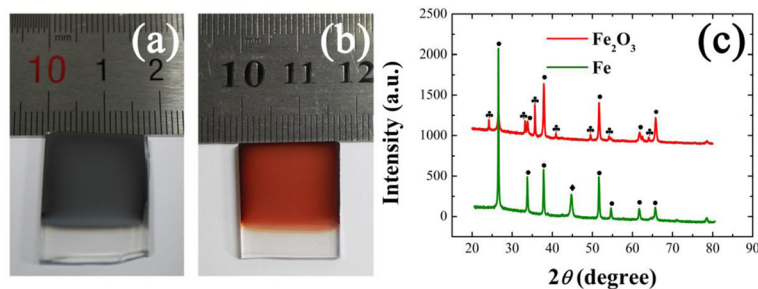
Liu *et al. Nanoscale Research Letters* (2015) 10:374

Page 3 of 8

Fig. 1 Digital photographs of **a** Fe and **b** α-Fe$_2$O$_3$ films on the FTO glass; **c** XRD patterns of Fe and α-Fe$_2$O$_3$ films

of Fe shows the body-centered cubic structure of Fe crystal (JCPDF No. 00-006-0696). The post annealing process converted Fe to hematite structure completely, where the peaks at 35.7°, 33.2°, and 24.2° correspond to the (101), (104), and (012) plane of hematite, respectively (JCPDF No. 33-0664).

Figure 2 shows the top and cross-sectional view of α-Fe$_2$O$_3$ on the FTO. The thickness of α-Fe$_2$O$_3$ film was increased from 180 to 270 nm with electrodeposition time increase from 120 to 360 s (Fig. 2b, c). The Fe film formation by electrodeposition is a chemical equilibrium between the chemical dissolution of Fe in the acid deposition solution and the deposition of Fe on the FTO, which is accomplished only as the deposition rate is higher than the surface dissolution rate [24]. The nanowire arrays with diameter of ~40 nm were found to exist uniformly on the surface of oxide thin film. The formation of surface nanowires is ascribed to the vapor-solid oxidation approach on Fe films, which has been reported to be a useful method for vertical growth of α-Fe$_2$O$_3$ nanowires or nanorods [25].

Figure 3 shows the surface morphology of Fe$_2$O$_3$-Au electrodes with different Au sputtering time. It was found that the diameter of Au NPs increases with the sputtering time. The Au NPs sputtered for 10 s are not homogeneous distributed with diameter ranging from 2 to 20 nm (see Fig. 3a). The sample with Au sputtered for 15 s shows the best homogeneous distribution of NPs with diameter of 10 ± 1 nm (see Fig. 3b). Some NPs on the nanowires can also be observed. The Fe$_2$O$_3$-Au with Au sputtered for 25 s shows the Au diameters with the range of 7–18 nm, while the diameter of sample with Au sputtered for 35 s is up to 40 nm which can be clearly observed in Fig. 3d.

The linear sweeps voltammetry (LSV) curves of the pristine Fe$_2$O$_3$ electrodes with varying deposition durations are shown in Fig. 4a. The photocurrent of the Fe$_2$O$_3$ electrode with deposition time for 180 s is the highest of all above –0.15 V vs Ag/AgCl. When the deposition time is 120 s, the thickness of film is ~180 nm (seen in Fig. 2b) which is too thin to absorb sufficient light. As the deposition time increases to 360 s, the
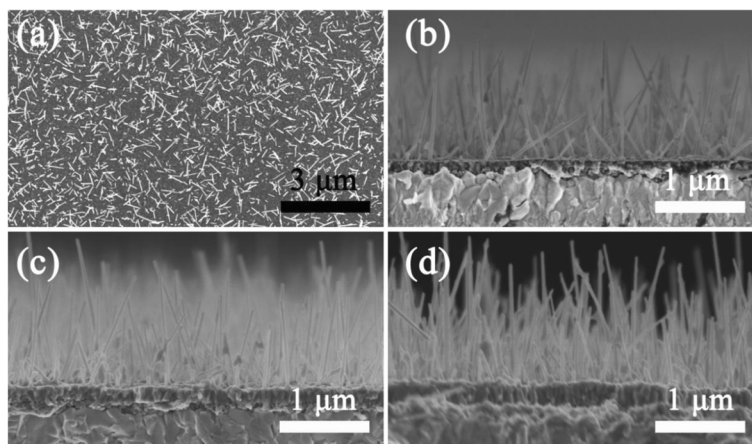

Fig. 2 a Top view of α-Fe$_2$O$_3$ with electrodeposition time of 180 s; cross-sectional view of α-Fe$_2$O$_3$ with different deposition time **b** 120 s; **c** 180 s; **d** 360 s, the electrodeposition current is 20 mA·cm^{-2}
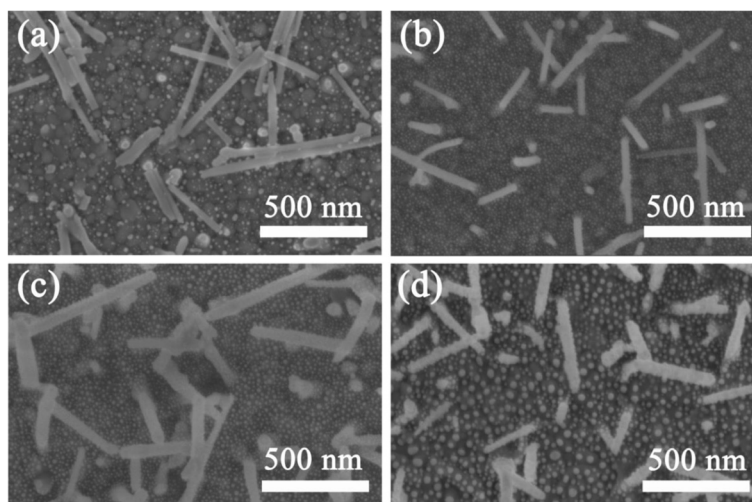
Fig. 3 Surface morphology of Fe_2O_3-Au electrodes with different Au sputtering time. **a** 10 s; **b** 15 s; **c** 25 s; **d** 35 s. The sputtering current is 30 mA·cm^{-2}. All electrodes are annealed at 300 °C for 1 h after the sputtering of Au

photocurrent is even lower, as seen from the Fig. 4a. The short hole diffusion length (~2–4 nm) [9] allows only holes created close to the electrolyte interface to oxidize water. Since the light penetration length in α-Fe_2O_3 is of the order of 100 nm [26], most holes created in the bulk will recombine with electrons before

reaching the surface as the thickness of Fe_2O_3 film increases to 270 nm (see Fig. 3d). In this regard, the following α-Fe_2O_3 photoelectrodes are studied based on 180 s deposition unless otherwise stated.

The LSV curves of the α-Fe_2O_3 electrodes with different Au sputtering durations are shown in Fig. 4b. The
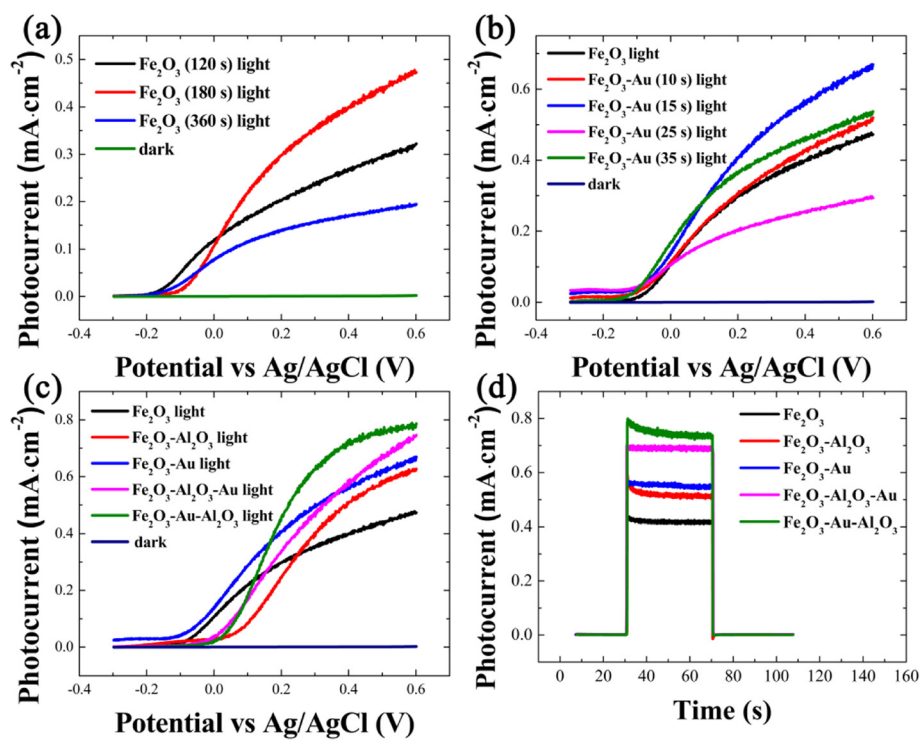

Fig. 4 LSV curves of **a** pristine Fe_2O_3 electrode with varying deposition time, **b** pristine Fe_2O_3 and Fe_2O_3-Au electrodes with different Au sputtering time, and **c** pristine Fe_2O_3 and modified Fe_2O_3. **d** Photocurrent responses of pristine Fe_2O_3 and modified Fe_2O_3 at an applied potential of 0.4 V. Electrolyte, 1 M KOH solution, illumination: a 300 W Xe lamp coupled with an AM 1.5 filter

Liu *et al. Nanoscale Research Letters* (2015) 10:374

Page 5 of 8

Fe_2O_3-Au (15 s) shows the best PEC performance among these electrodes above 0.1 V vs Ag/AgCl. It may be resulted from the particle size and the distribution variations for the different Fe_2O_3-Au samples, which changes the resonance frequency and intensity of Au SPR peaks [27]. As the nanoparticles are smaller than 3 nm, the SPR could not be motivated due to the quantum confinement effect [28]. The SPR begins to work as the nanoparticles increase to be larger than 4 nm, and the resonance will be red shifted with the size increase of metal nanoparticles. The spectra overlap between plasmonic Au nanoparticles, and Fe_2O_3 may happen on the proper Au nanoparticles morphology. Additionally, the metal nanoparticles absorb photons from an area much larger than their geometric cross section [29]. The photon absorption by Fe_2O_3 itself may be decreased with the excessive size increase of metal particles. According to the experimental results, 15 s was thus chosen as the sputtering time for the following Au deposition.

Le Formal et al. [23] demonstrated an enhancement of photocurrent in comparison with the Fe_2O_3 electrode by employing Al_2O_3 passivation coating. The Al_2O_3 surrounding also results in an increase of dielectric circumstance of metal nanoparticles, which could strengthen the localized electromagnetic field with tunable resonance frequency [30, 31]. Therefore, a combination of NPs and Al_2O_3 coating is of special interest in PEC system. For comparison, the modified Fe_2O_3 electrodes with both single step coating (i.e., Fe_2O_3-Al_2O_3 and Fe_2O_3-Au) and sequential coating (Fe_2O_3-Au-Al_2O_3 and Fe_2O_3-Al_2O_3-Au) processes are characterized. Figure 4c shows that the photocurrent of the pristine Fe_2O_3-Au electrodes is obviously higher than others at 0.0 V vs Ag/AgCl, which could be attributed to the increased open circuit potential by the Au modification. The hematite films are n-type photoanodes and a positive applied bias potential will increase the photocurrent generation as the Fermi level moves to assist charge separation and facilitate water splitting [32]. The conduction band of α-Fe_2O_3 is located slightly below the level needed for hydrogen production, and its valence band is well-suited for oxygen production. Therefore, an external bias is typically required for water splitting when using α-Fe_2O_3 materials as photoanodes [26, 33]. The photocurrent of the samples increases unceasingly at a higher potential, and the photocurrent of the Fe_2O_3-Au-Al_2O_3 electrode increases to 1.78-fold compared to that of the pristine Fe_2O_3 at the potential of 0.4 V. The trend of photocurrent responses measured at an applied potential of 0.4 V in Fig. 4d mirrors that of the LSV plots, which follows the order of Fe_2O_3-Au-Al_2O_3 > Fe_2O_3-Al_2O_3-Au > Fe_2O_3-Au > Fe_2O_3-Al_2O_3 > Fe_2O_3.

The Mott-Schottky and Nyquist plots are used to determine the carrier density, capacitance, and impedance of the electrodes, and the results are shown in Fig. 5. Carrier density can be calculated from the slope of Mott-Schottky plots. The equation is shown as follows:

$$N_d = \frac{2}{e_0 \varepsilon \varepsilon_0 \frac{d\left(\frac{1}{C^2}\right)}{dV}}$$

Where e_0 is the electron charge, ε is the dielectric constant of Fe_2O_3 ($\varepsilon = 80$) [34, 35], ε_0 is the permittivity of vacuum, N_d is the donor density, and V is the applied bias at the electrode. The positive slopes indicate the n-type behaviors of both pristine and modified samples. The calculated electron density of electrodes is shown in the Fig. 5b. The electron density of Fe_2O_3-Au-Al_2O_3 is 4.61×10 cm^{-3} [17], which is 120 times of that of pristine Fe_2O_3 electrode. Then, the interfacial properties between the electrolyte and electrodes are further characterized by electrochemical impedance spectroscopy (EIS) under dark condition (Fig. 5c). The arc of Nyquist plot is characteristic of charge transportation resistance. The diameter of the arc for the Fe_2O_3-Au-Al_2O_3 electrode is the smallest one, indicating that the resistance of the charge transportation is significantly decreased. The diameter of the arc for these electrodes follows the order of Fe_2O_3-Au-Al_2O_3 < Fe_2O_3-Al_2O_3-Au $\approx$ Fe_2O_3-Al_2O_3 < Fe_2O_3-Au < Fe_2O_3. The small arc diameter of Al_2O_3 coated Fe_2O_3-based electrode indicates the facilitated charge transportation enhanced by the decreased surface recombination from Al_2O_3 passivation.

The FDTD simulations were performed to calculate electric field distribution across the interfaces in different electrodes under 574 nm as shown in Fig. 6. The color index represents the magnitude of electric field intensity normalized with that of the light propagating in free space. The electric field intensity of pristine Fe_2O_3 and Fe_2O_3-Al_2O_3 electrodes is very weak under 574 nm, and there is no change in color on the interface (not shown here). As coupling the Au plasmonic structure and Al_2O_3 coating on Fe_2O_3 electrode, high-electric field intensity can be always found in the area where the Au is in contact with semiconductor and Al_2O_3. It is generally accepted that there are three non-mutually exclusive energy-transfer mechanisms in plasmonic-photocatalyst systems, involving the SPR-induced charge injection from metal to semiconductor, near-field electromagnetic, and scattering mechanism [29]. The scattering effect can be safely ruled out in our study because it usually occurs in plasmonic metal nanostructures with the diameter larger than 50 nm. SPR-induced charge injection and near-field electromagnetic mechanism may co-contribute on our Fe_2O_3-Au systems. In near-field electromagnetic mechanism, the excited Au increases the intensity of local electric field, which will penetrate into Fe_2O_3 and amplify the local light intensity. For the Fe_2O_3-Al_2O_3-Au

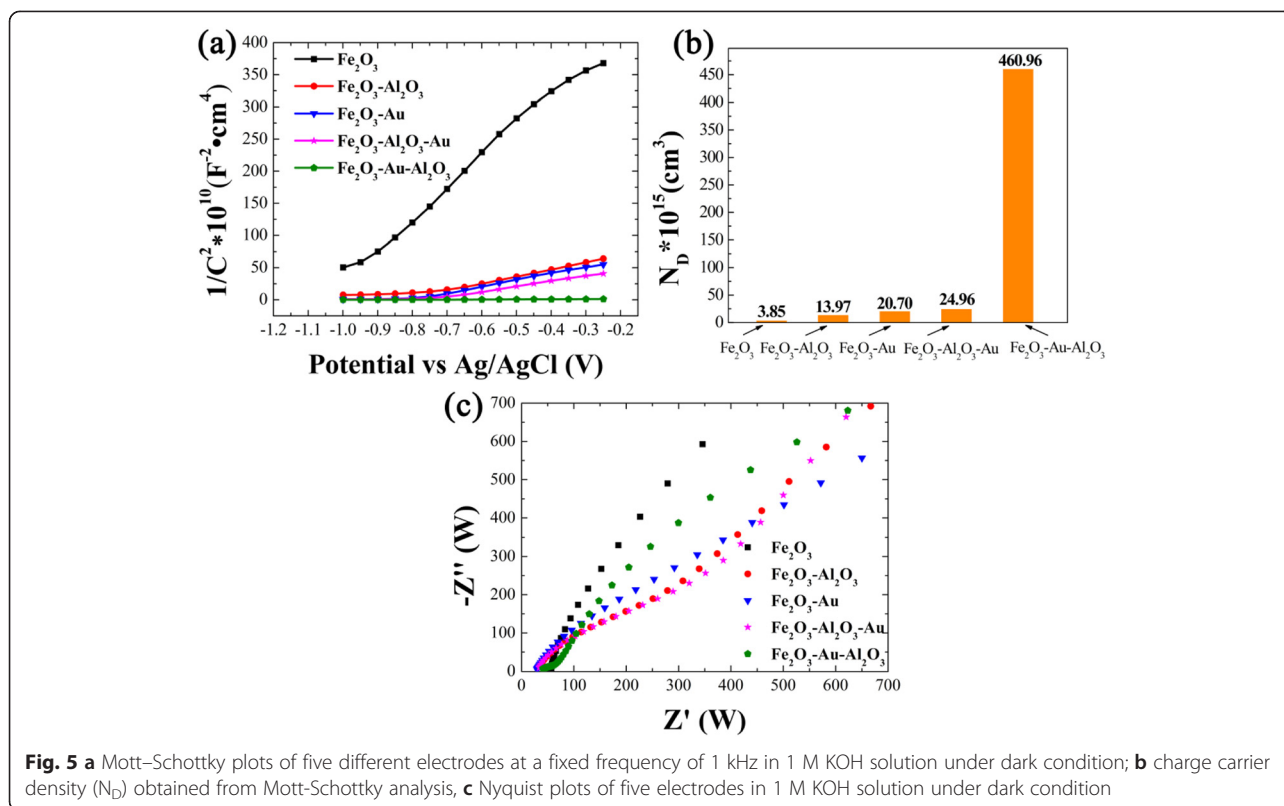Liu *et al. Nanoscale Research Letters* (2015) 10:374

Page 6 of 8

Fig. 5 a Mott–Schottky plots of five different electrodes at a fixed frequency of 1 kHz in 1 M KOH solution under dark condition; **b** charge carrier density (N_D) obtained from Mott-Schottky analysis, **c** Nyquist plots of five electrodes in 1 M KOH solution under dark condition

electrode, the intensified electromagnetic field is largely blocked by the Al_2O_3 spacer layer. This suggests that the near-field electromagnetic enhancement mechanism can hardly contribute the enhanced PEC performance with the presence of dielectric spacer layer, which is in accordance with our previous work [16]. Despite this, the Fe_2O_3-Al_2O_3-Au electrode still shows the higher photocurrent than Fe_2O_3-Al_2O_3 electrode, which could benefit from the SPR-mediated hot-electron injection process. The Fe_2O_3-

Au-Al_2O_3 electrode shows the strongest LSPR electric field, biggest radiation areas, and deepest penetration depth into the Fe_2O_3 (Fig. 6c), as compared with the other configurations. This may be mainly resulted from the fact that the Al_2O_3 coating increases the refractive index of the surrounding medium from 1.33 (in water) to 1.76 (in Al_2O_3) [36, 37], which could intensify the plasmon resonance. Both near-field electromagnetic effect and SPR-induced charge injection from metal to semiconductor
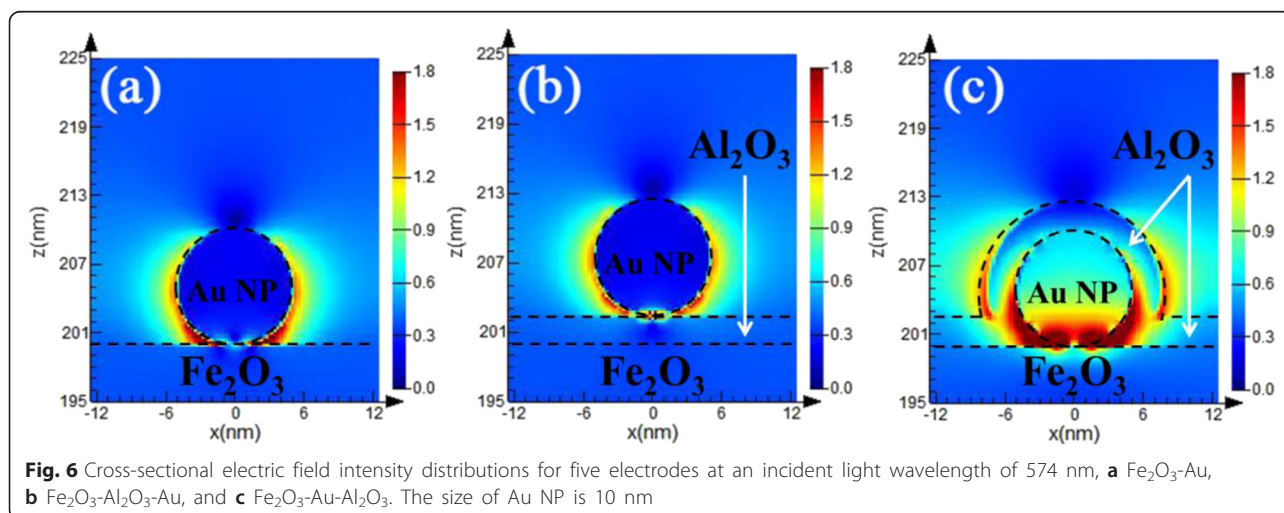

Fig. 6 Cross-sectional electric field intensity distributions for five electrodes at an incident light wavelength of 574 nm, **a** Fe_2O_3-Au, **b** Fe_2O_3-Al_2O_3-Au, and **c** Fe_2O_3-Au-Al_2O_3. The size of Au NP is 10 nm

Liu *et al. Nanoscale Research Letters* (2015) 10:374

Page 7 of 8

could contribute the intensified electric field and the enhanced PEC performances. The rate of electron–hole formation is proportional to the local intensity of the electric field and radiation areas [38]. It means that more pairs of electron–hole are generated in the Fe_2O_3 semiconductor, which is in accordance with the much increased ND value in the Mott-Schottky analysis (see Fig. 5). Consequently, most of the photogenerated charges created by the plasmon excitation contribute to the surface catalysis for water splitting. From the perspective of the SPR-mediated hot-electron injection mechanism, the intensified electromagnetic field will facilitate more energetic electrons on Au nanoparticles. Electrons photoexcited by the Au NPs will pass over the Schottky barrier and migrate to the conduction band of Fe_2O_3. Schottky barrier at the interface also helps the transferred hot electrons accumulate in the Fe_2O_3 conduction band, preventing them from traveling back to the Au NPs.

Conclusions

The thin film α-Fe_2O_3 electrodes with surface nanowire were successfully obtained by electrodeposition and post thermal annealing process for PEC water-splitting application. The LSPR of Au NPs in conjunction with surface passivation by Al_2O_3 shells was further introduced for the enhanced PEC performance of α-Fe_2O_3 photoelectrodes. Among the different configurations, the Fe_2O_3-Au-Al_2O_3 construction shows the best PEC performance, attributing to the Al_2O_3 intensified LSPR, effective surface passivation by Al_2O_3 surface coating, and the rapid charge carriers transfer due to the Schottky junctions at the interface of metal and semiconductor. These results can not only contribute fundamentally to the mechanism studies of the SPR-based photocatalysis but also open a new avenue for the design strategies of high-performance photocatalysts for solar-to-fuel energy conversion.

Competing interests
The authors declare that they have no competing interests.

Author's contributions
YTL carried out the experiments and drafted the manuscript. ZX carried out the simulation and the experimental analysis. MY participated in the statistical analysis and helped to polish the manuscript. HWF and WJC helped the electrochemical experiments. LFL conceived the study and helped to polish the manuscript. YS participated in the experimental design. JM and XFZ conceived the study and participated in its design and coordination. All authors read and approved the final manuscript.

Author details
[1]Key Laboratory of Soft Chemistry and Functional Materials of Education Ministry, Nanjing University of Science and Technology, Nanjing 210094, China. [2]Shanghai Advanced Research Institute, Chinese Academy of Sciences, Shanghai 201210, China. [3]School of Environmental and Chemical Engineering, Shanghai University, Shanghai 200444, China.

References
1. Turner JA. A realizable renewable energy future. Science. 1999;285(5428):687–9.
2. Kondofersky I, Dunn HK, Muller A, Mandlmeier B, Feckl JM, Fattakhova-Rohlfing D, et al. Electron collection in host-guest nanostructured hematite photoanodes for water splitting: the influence of scaffold doping density. ACS Appl Mater Interfaces. 2015;7(8):4623–30.
3. Sliozberg K, Stein HS, Khare C, Parkinson BA, Ludwig A, Schuhmann W. Fe-Cr-Al containing oxide semiconductors as potential solar water-splitting materials. ACS Appl Mater Interfaces. 2015;7(8):4883–9.
4. Osterloh FE. Inorganic materials as catalysts for photochemical splitting of water. Chem Mater. 2008;20(1):35–54.
5. Qiu YC, Leung SF, Zhang QP, Hua B, Lin QF, Wei ZH, et al. Efficient photoelectrochemical water splitting with ultrathin films of hematite on three-dimensional nanophotonic structures. Nano lett. 2014;14(4):2123–9.
6. Murphy A, Barnes P, Randeniya L, Plumb I, Grey I, Horne M, et al. Efficiency of solar water splitting using semiconductor electrodes. Int J Hydrogen Energ. 2006;31(14):1999–2017.
7. Cherepy NJ, Liston DB, Lovejoy JA, Deng H, Zhang JZ. Ultrafast studies of photoexcited electron dynamics in γ-and α-Fe_2O_3 semiconductor nanoparticles. J Mater Chem B. 1998;102(5):770–6.
8. Joly AG, Williams JR, Chambers SA, Xiong G, Hess WP, Laman DM. Carrier dynamics in α-Fe_2O_3 (0001) thin films and single crystals probed by femtosecond transient absorption and reflectivity. J Appl Phys. 2006;99(5):053521.
9. Khaselev O, Turner JA. A monolithic photovoltaic-photoelectrochemical device for hydrogen production via water splitting. Science. 1998;280(5362):425–7.
10. Kennedy J, Frese Jr KW. Photooxidation of water at α-Fe_2O_3 electrodes. J Electrochem Soc. 1978;125(5):709–14.
11. Atwater HA, Polman A. Plasmonics for improved photovoltaic devices. Nat Mater. 2010;9(3):205–13.
12. Standridge SD, Schatz GC, Hupp JT. Distance dependence of plasmon-enhanced photocurrent in dye-sensitized solar cells. J Am Chem Soc. 2009;131(24):8407–9.
13. Link S, El-Sayed MA. Size and temperature dependence of the plasmon absorption of colloidal gold nanoparticles. J Phys Chem B. 1999;103(21):4212–7.
14. Niu WB, Li X, Karuturi SK, Fam DW, Fan H, Shrestha S, et al. Applications of atomic layer deposition in solar cells. Nanotechnology. 2015;26(6):064001.
15. Chandiran AK, Yella A, Stefik M, Heiniger LP, Comte P, Nazeeruddin MK, et al. Low-temperature crystalline titanium dioxide by atomic layer deposition for dye-sensitized solar cells. ACS Appl Mater Interfaces. 2013;5(8):3487–93.
16. Xu Z, Lin YY, Yin M, Zhang HF, Cheng CW, Lu LF, et al. Understanding the enhancement mechanisms of surface plasmon-mediated photoelectrochemical electrodes: a case study on Au nanoparticle decorated TiO_2 nanotubes. Adv Mater Interfaces. 2015. doi:10.1002/admi.201500169.
17. Gui QF, Xu Z, Zhang HF, Cheng CW, Zhu XF, Yin M, et al. Enhanced photoelectrochemical water splitting performance of anodic TiO_2 nanotube arrays by surface passivation. ACS Appl Mater Interfaces. 2014;6(19):17053–8.
18. Paracchino A, Laporte V, Sivula K, Grätzel M, Thimsen E. Highly active oxide photocathode for photoelectrochemical water reduction. Nat Mater. 2011;10(6):456–61.
19. Hwang YJ, Hahn C, Li B, Yang PD. Photoelectrochemical properties of TiO_2 nanowire arrays: a study of the dependence on length and atomic layer deposition coating. Acs Nano. 2012;6(6):5060–9.
20. Yang CY, Qin Y, Zhu XF, Yin M, Li DD, Chen XY, et al. Inverted nanotaper-based Ag film for optical absorption and SERS applications. J alloy compd. 2015;632:634–8.
21. Bechelany M, Maeder X, Riesterer J, Hankache J, Lerose D, Christiansen S, et al. Synthesis mechanisms of organized gold nanoparticles: influence of annealing temperature and atmosphere. Cryst Growth Des. 2010;10(2):587–96.
22. Xu C, Song Y, Lu LF, Cheng CW, Liu DF, Fang XH, et al. Electrochemically hydrogenated TiO_2 nanotubes with improved photoelectrochemical water splitting performance. Nanoscale Res Lett. 2013;8(1):1–7.

Liu *et al. Nanoscale Research Letters* (2015) 10:374

Page 8 of 8

23. Le Formal F, Tétreault N, Cornuz M, Moehl T, Grätzel M, Sivula K. Passivating surface states on water splitting hematite photoanodes with alumina overlayers. Chem Sci. 2011;2(4):737–43.

24. Zeng QY, Bai J, Li JH, Xia LG, Huang K, Li XJ, et al. A novel in situ preparation method for nanostructured α-Fe$_2$O$_3$ films from electrodeposited Fe films for efficient photoelectrocatalytic water splitting and the degradation of organic pollutants. J Mater Chem A. 2015;3(8):4345–53.

25. Zhong ML, Liu ZW, Zhong XC, Yu HY, Zeng DC. Thermal growth and nanomagnetism of the quasi-one dimensional iron oxide. J Mater Sci Technol. 2011;27(11):985–90.

26. Lin Y, Zhou S, Sheehan SW, Wang D. Nanonet-based hematite heteronanostructures for efficient solar water splitting. J Am Chem Soc. 2011;133(8):2398–401.

27. Liu X, Yang Y, Mao LG, Li ZJ, Zhou CJ, Liu XH, et al. SPR quantitative analysis of direct detection of atrazine traces on Au-nanoparticles: nanoparticles size effect. Sensor Actuat B-Chem. 2015;218:1–7.

28. Kim TW, Cho CH, Kim BH, Park SJ. Quantum confinement effect in crystalline silicon quantum dots in silicon nitride grown using SiH$_4$ and NH$_3$. Appl Phys Lett. 2006;88(12):123102.

29. Warren SC, Thimsen E. Plasmonic solar water splitting. Energy Environ Sci. 2012;5(1):5133–46.

30. Miller MM, Lazarides AA. Sensitivity of metal nanoparticle surface plasmon resonance to the dielectric environment. J Phys Chem B. 2005;109(46):21556–65.

31. Tam F, Moran C, Halas N. Geometrical parameters controlling sensitivity of nanoshell plasmon resonances to changes in dielectric environment. J Phys Chem B. 2004;108(45):17290–4.

32. Kleiman-Shwarsctein A, Hu Y, Forman AJ, Stucky JK, McFarland EW. Electrodeposition of α-Fe$_2$O$_3$ doped with Mo or Cr as photoanodes for photocatalytic water splitting. J Phys Chem C. 2008;112(40):15900–7.

33. Kay A, Cesar I, Grätzel M. New benchmark for water photooxidation by nanostructured α-Fe$_2$O$_3$ films. J Am Chem Soc. 2006;128(49):15714–21.

34. Cesar I, Sivula K, Kay A, Zboril R, Graetzel M. Influence of feature size, film thickness, and silicon doping on the performance of nanostructured hematite photoanodes for solar water splitting. J Phys Chem C. 2009;113(2):772–82.

35. Goncalves RH, Lima BH, Leite ER. Magnetite colloidal nanocrystals: a facile pathway to prepare mesoporous hematite thin films for photoelectrochemical water splitting. J Am Chem Soc. 2011;133(15):6012–9.

36. Miller MM, Lazarides AA. Sensitivity of metal nanoparticle plasmon resonance band position to the dielectric environment as observed in scattering. J Opt A: Pure Appl Opt. 2006;8(4):S239–49.

37. Lee KS, El-Sayed MA. Gold and silver nanoparticles in sensing and imaging: Sensitivity of plasmon response to size, shape, and metal composition. J Phys Chem B. 2006;110(39):19220–5.

38. Lee J, Javed T, Skeini T, Govorov AO, Bryant GW, Kotov NA. Bioconjugated Ag nanoparticles and CdTe nanowires: Metamaterials with field-enhanced light absorption. Angew Chem Int Edit. 2006;45(29):4819–23.